

Controlled Dy-doping to Nickel-rich Cathode Materials in High Temperature Aerosol Synthesis

Chao Yan^{1*}, Xiaofang Yang^{2*}, Hao Zhao¹, Hongtao Zhong¹, Guoming Ma¹, Yongfeng Qi¹, Bruce E. Koel², and
Yiguang Ju¹

¹ Department of Mechanical and Aerospace Engineering, Princeton University, Princeton, NJ, 08544, USA

² Department of Chemical and Biological Engineering, Princeton University, Princeton, NJ, 08544, USA

*Corresponding author: Chao Yan

Email: Chaoy@princeton.edu

Address: Department of Mechanical and Aerospace Engineering, Princeton University, Princeton, NJ, 08544,
USA

*Corresponding author: Xiaofang Yang

Email: Xiaofang@princeton.edu

Address: Department of Chemical and Biological Engineering, Princeton University, Princeton, NJ, 08544, USA

Colloquium: New concepts

Total length: 5688

Main text: 3024

References: 368

Table 1: 183

Table 2: 183

Figure 1 with caption: 377

Figure 2 with caption: 171

Figure 3 with caption: 555

Figure 4 with caption: 234

Figure 5 with caption: 153

Figure 6 with caption: 275

Figure 7 with caption: 165

List of Figure Captions

Figure 1. SEM images of precursors and annealed cathode materials: A) pristine NCM811 precursor; B) 1.5% Dy-doped NCM811 precursor; C) 3%-Dy doped NCM811 precursor; D) pristine NCM811-800 °C; E) 1.5% Dy-doped NCM811-800 °C; and F) 3% Dy-doped NCM811-800 °C.

Figure 2. XRD of pristine NCM811, 1.5% Dy, and 3% Dy. The impurity peaks (labeled by *) is due to the presence of LiDyO₂ monoclinic phase. X-ray: Ag K α .

Figure 3. Region scans of XPS spectra for Ni2p, Co2p, Mn2p and Dy 3d for pristine (black), 1.5% Dy-doped (blue), and 3% Dy-doped (red) samples.

Figure 4. Initial charge/discharge curves (A) and long-term performance (B) of pristine NCM811 (red), 1.5% Dy-800°C (blue), and 3% Dy-800°C (black).

Figure 5. Rate performance of pristine NCM811 (Red), 1.5% Dy-800°C (Blue), and 3% Dy-800°C (Black). Rates: 0.1C, 0.2C, 0.5C, 1C, 2C, and 5C. The rate charge-discharge curves are shown in supporting Figure S4.

Figure 6. Cyclic voltammetry (A) and impedance spectra (B) of pristine NCM811 (red), 1.5% Dy-800°C (blue). Scan rate: 0.1C, Voltage range: 2.5-4.5 V. Impedance: at 4.2 V with 5 mV modulation. Frequency: 0.1-100 kHz.

Figure 7. Thermal decomposition profile of charged pristine and 1.5% Dy-doped NCM811.

Abstract

Layered nickel-rich materials are promising next-generation cathode materials for lithium ion batteries due to their high capacity and low cost. However, the poor thermal stability and longtime cycling performance hinders the commercial applications of high nickel materials. Doping with heteroatoms has been an effective approach for improving electrochemical performance of cathode materials. Controlling doping concentration and geometrical distribution is desired for optimal electrochemical performance, but it is challenging in traditional co-precipitation methods. In this work, controlled dysprosium (Dy) doping to NCM811 was studied in an aerosol synthesis method by controlling the precursor concentrations and heating parameters. The obtained materials were characterized by SEM, XRD, and XPS, and their electrochemical properties and thermal stability were evaluated. By controlling the doping concentration (1.5%), Dy-doped NCM811 was improved simultaneously in long-term cycling and high-rate performance. The thermal-chemical stability of the Dy-doped cathode materials was examined in a microflow reactor with a mass spectrometer. The results showed that Dy-doping shifted the O₂ onset temperature to a higher temperature and reduced O₂ release by 80%, thus dramatically increasing the thermal-chemical stability and improving the fire safety of cathode materials. Since high temperature aerosol synthesis is a low-cost and scalable method, the findings in this work have broad implications for commercial synthesis of novel materials with controlled doping modification to achieve high electrochemical performance and safety in lithium ion batteries.

Keywords: lithium ion battery; dysprosium (Dy) doping; cathode materials; high temperature synthesis; thermal stability

1. Introduction

Li-ion batteries (LIBs) have been used extensively in electric vehicles and hybrid electrical vehicles because of their high energy density and high power capability. [1-3] [ENREF 2](#) The main limiting factor of advanced Li-ion batteries is still the cathode, which determines the energy density, cycle life, stability, and safety features. [4] Recently, to achieve high-performance cathode materials with high energy density and power density, Ni-rich ternary materials such as $\text{LiNi}_{0.8}\text{Co}_{0.1}\text{Mn}_{0.1}\text{O}_2$ (NCM811) are attractive because of their high capacity and low cost. [5] Although the energy density increases with increasing Ni ratio, the long-term cycling performance and safety of these Ni-rich cathode materials becomes worse and needs to be significantly improved to meet the requirements from industry. [5] Accordingly, modifying the chemical and physical properties of the Ni-rich materials has been attempted to improve the electrochemical performance. [6] Surface coating and bulk doping are two common approaches to increase the cycling performance and thermal stability at high temperatures. [7-9] [ENREF 9](#) [ENREF 8](#) In order to achieve desirable properties, the coating thickness, morphology and crystallinity has been carefully controlled, which is complicated and requires additional costs in cathode production.[9]

Doping is useful to improve the cycle stability and rate performance for the cathode material; however, this usually causes capacity fading because of the introduction of inactive elements. [10] Currently, a large number of different kinds of ions have been studied as dopants to cathode materials. [7] Previous studies revealed that rare earth element doping (La, Ce, Pr) can affect the structure and electrochemical properties of $\text{LiNi}_{0.33}\text{Co}_{0.33}\text{Mn}_{0.33}\text{O}_2$ (NCM111) and $\text{LiNi}_{0.5}\text{Co}_{0.2}\text{Mn}_{0.3}\text{O}_2$ (NCM523) for lithium-ion batteries. [11, 12] [ENREF 10](#) In this paper, we focus on studying the doping effect of Dysprosium (Dy) in a nickel-rich layered structured cathode material, NCM811, on the electrochemical performance and thermal stability. Dysprosium is a rare earth element in the row of Lanthanides, which has not been explored as a dopant for cathode materials in lithium ion batteries. The common oxidation state of Dy is 3+, corresponding to 9 electrons in the f shell. High coordination numbers of 9-12 are often observed in the lanthanide compounds. [13] The doping of Dy into the lattice of Ni oxide compounds may cause interesting changes to the structure, thereby influencing the electrochemical performance. [11] In this work, Dy has been successfully doped in the NCM811 by using high temperature aerosol synthesis with controlled doping concentrations (1.5% and 3%). Such modification is found to significantly improve the long-term cycling

performance of high-Ni materials and this improvement can be attributed to stabilizing the crystal structure and reducing charge transport resistance by Dy doping. In addition, the Dy doped high-Ni material demonstrates improved thermal-chemical stability.

2. Experimental section

2.1. Synthesis of NCM 811 and Dy-doped NCM 811

Ni-rich cathode materials are synthesized in a high temperature aerosol-pyrolysis reactor, which consists of two heat-controlled regions: i) a low temperature preheating region, and ii) a high-temperature flame decomposition region. The details of a similar home-made reactor and other information on the material synthesis have been described in our previous paper [14] and in the supporting information (Figure S1). Briefly, the precursor solution was prepared by dissolving Ni, Co, Mn and Li nitrates in distilled water. A home-made ultrasonic atomizer (2.4 M Hz) was used to generate aerosols particles at the bottom of the reactor. After preheating, solid spherical particles can generally be obtained at low temperatures (100-150 ° C) over a relatively long heating time (5-10 seconds). After preheating, dry aerosol particles passed through a high temperature flame (< 1400 °C) zone for further decomposition of precursor compounds. Then, the collected powders were further annealing in a tube furnace for sintering under constant O₂ flow. This additional annealing step is critical as it improves the crystallinity and reduces the ion mixing in the crystal structure of NCM811.

2.2. Electrochemical measurement

CR2032 coin-type cells were utilized to examine the electrochemical properties of all cathode samples. The preparation of the cathode electrodes and battery assembling are discussed in the supporting information. The electrochemical test was performed between 2.8 and 4.3 V (vs. Li/Li⁺) at 25 °C by using a Neware Instrument (CT-3008) after aging for 24 h. Cyclic voltammograms (CVs) were measured between 2.5 and 4.3 V at 0.1 mV s⁻¹ by using a Pine electrochemical workstation. EIS was performed by using a Pine electrochemical workstation with a frequency range between 100 kHz and 0.01 Hz.

2.3. High-resolution X-ray photoelectron spectroscopy (HRXPS)

HRXPS analysis of the NCM811 cathode samples was conducted using a ThermoFisher K-Alpha X-ray Photoelectron Spectrometer. Survey spectra was taken at 200 eV pass energy and the high resolution spectra for the C1s, O1s, Ni2p, Co2p, Mn2p, and Dy3d regions were recorded at 50 eV pass energy. The C1s peak position in these measurements was at 284.7 ± 0.1 eV binding energy. The chemical compositions were determined using CasaXPS (Casa Software Ltd.) fitting software.

2.4. *X-ray powder diffraction (XRD)*

The crystal structure of the synthesized samples was probed by X-ray powder diffraction (XRD, Bruker-8), with Ag- K_{α} radiation in the 2θ range from 3° to 30° at $1^{\circ}/\text{min}$.

2.5. *High-resolution scanning electron microscopy (HR-SEM) and energy dispersive X-ray spectroscopy (EDX)*

HR-SEM, performed on a Verios 460 Extreme High Resolution SEM (XHR-SEM), was utilized to characterize the cathode materials before and after sintering at different temperatures. An Oxford EDX spectrometer, installed inside the SEM chamber, was utilized for element mapping and analysis. The SEM images were obtained using a beam at 3-5 kV and 50 pA.

2.6. *Thermal-Chemical Stability*

Thermal-chemical stability of cathode materials was evaluated by temperature programmed reaction (TPR) measurement. During the thermal-chemical stability experiment, the temperature of the charged cathode materials was controlled to linearly increase from 30 to 700°C with a heating rate of $5^{\circ}\text{C min}^{-1}$. A constant Ar flow of 50 ml min^{-1} was used to purge the quartz tube and the reaction products were detected by the mass spectrometer (see supporting Figure S2 for details of the set-up).

3. **Results and Discussion**

3.1. *Cathode material synthesis and characterization*

Morphologies and sizes of the particles in aerosol synthesis are normally controlled by the evaporation rate of the solvent and decomposition temperatures. Recently, we investigated the effect of droplet size and synthesis temperature on the particle formation pathway by comparing micron-sized droplets (average diameter $3.5 \mu\text{m}$) produced by ultrasonic atomization. It has been found that the particle morphology is strongly determined by the

ratio of solvent evaporation time to solute diffusion time (τ_{evap}/τ_{diff}). By controlling τ_{evap}/τ_{diff} for uniform heating of the aerosol droplets, the formation of solid particles can be achieved. [15] As shown in Figure 1A-C, the precursor particles of NCM811 are spherical with the diameters in the range of 0.3-1.5 μm . Similar particle sizes and morphologies were observed for the Dy-doped samples. The synthesized precursor particles are further annealed in O_2 gas for 12 h. This step is used to improve the material crystallinity and to form the layered structure crystal phase. As shown in Figure 1E-F, the spherical shape of the precursor particles completely disappeared after sintering in O_2 at high temperatures. Instead, single crystal primary structures with sizes of 200-600 nm appeared and porous and irregularly shaped particles were formed. Although similar morphological evolution during high temperature annealing was observed for the Dy-doped NCM811 samples, the crystal size of the primary structure gradually increased with increasing Dy concentration. The elemental compositions of the particles were analyzed by EDX and the results are compared in Table 1. The mole ratios of Ni, Co, Mn and Dy in all the samples were consistent with the elemental compositions in the precursor solutions. EDX elemental mapping, as shown in Supporting Figure S3, indicates uniform doping of Dy in the NCM 811 material without any large Dy rich phase or domains present in the structure.

Table 1. Elemental compositions (Ni, Co, Mn and Dy, %) determined by EDX analysis for pristine NCM811, 1.5% Dy, and 3% Dy samples.

	Pristine NCM811	1.5 % Dy	3% Dy
Ni	80.2	78.2	78.1
Co	10.2	10.6	9.7
Mn	9.6	9.8	9.5
Dy	0	1.4	2.7

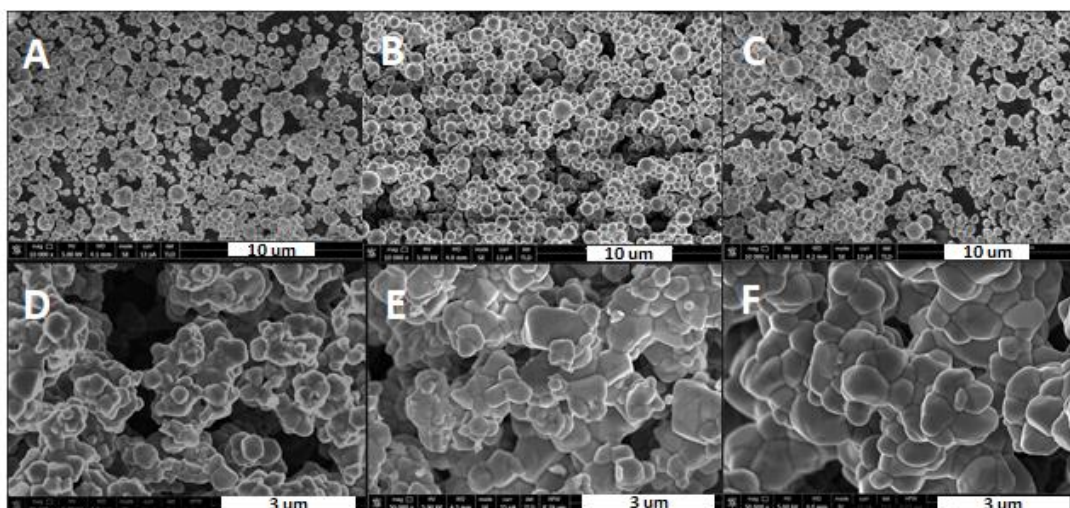


Figure 1. SEM images of precursors and annealed cathode materials: A) pristine NCM811 precursor; B) 1.5% Dy-doped NCM811 precursor; C) 3%-Dy doped NCM811 precursor; D) pristine NCM811-800 °C; E) 1.5% Dy-doped NCM811-800 °C; and F) 3% Dy-doped NCM811-800 °C.

The crystal structures of the precursors and annealed samples were examined by XRD and the results are compared in Figure 2. The diffraction patterns of the three samples are indexed to a layered hexagonal structure with the R3-m space group. The host structure was not changed after modification with Dy according to the XRD patterns. The splitting of the (006)/(012) and (018)/(110) peaks indicated a well-ordered layer structure for all samples. The degree of cation mixing can be obtained by the intensity ratio I of the (003) and (104) peaks ($I=I(003)/I(104)$), and cation mixing is normally considered not significant if the ratio is more than 1.2. The value of I for all samples was larger than 1.2, which indicates good ordering. Interestingly, the peak ratio increases from 1.23 for Dy-0 to 1.27 for Dy-1.5. Since the oxidation states of Dy and Ni are both 3+, doping with Dy^{3+} does not cause an increase in Ni^{2+} content due to charge compensation as observed for doping with higher charged ions such as Ce^{4+} and Zr^{4+} . This can be explained as some doped Dy^{3+} (0.91 a) occupation of Li^+ (0.90 a) sites due to the similar ionic radius, and suppression of the migration of Ni^{2+} from the TM layer to the Li layer, thus restraining cation mixing. As the amount of Dy^{3+} increased, the degree of cation mixing increased ($I=1.24$ for Dy-0.03). Due to the similar radius of Dy^{3+} (0.91 a) and Li^+ (0.90 a), Dy^{3+} can be doped into both the Li layer and the TM layer (Ni^{3+} sites). The doped Dy^{3+} in the Li layer could act as pillars to support the layer structure during the charge–discharge process, whereas Dy^{3+} in the TM layer could stabilize the crystal structure as a result of the

strong Dy-O bonds. Clearly, impurity phase-LiDyO₂ (monoclinic) was formed at 1.5% Dy doping and became obvious at 3% Dy doping.

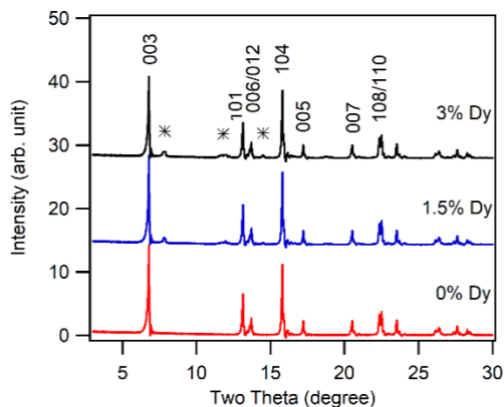


Figure 2. XRD of pristine NCM811, 1.5% Dy, and 3% Dy. The impurity peaks (labeled by *) is due to the presence of LiDyO₂ monoclinic phase. X-ray: Ag K α .

The surface composition and oxidation states were analyzed by XPS on both the pristine and Dy-doped samples. The fine scans of Ni2p, Co2p, Mn2p and Dy3d are shown in Figure 3. The results of the surface composition analysis are summarized in Table 2. Compared to the EDX elemental analysis of the bulk materials (Mn/Ni=0.12), a higher concentration of Mn with a Mn/Ni ratio of 0.26 is present at the surface of the 1.5% Dy-doped sample. This means the surface Ni concentration (69.5%) is smaller than it is in the bulk (78.2%) while the surface Co concentration is similar on the surface and in the bulk. The higher concentration of Mn observed at the surface than in the bulk indicates that there exists a core-shell or concentration gradient structure on the particle. The lower surface Ni concentration (or high surface Mn concentration) is beneficial to reducing the parasitic reactions between the cathode and the electrolyte. However, this Mn surface enrichment is not observed for the pristine sample. Higher concentration of Dy doping does not demonstrate a similar effect either. Only 5.2% Mn is present on the 3% Dy-doped sample surface. Thus, Dy doping affects ion precipitation and diffusion kinetics during the synthesis of the precursors and the detailed mechanism is not yet clear.

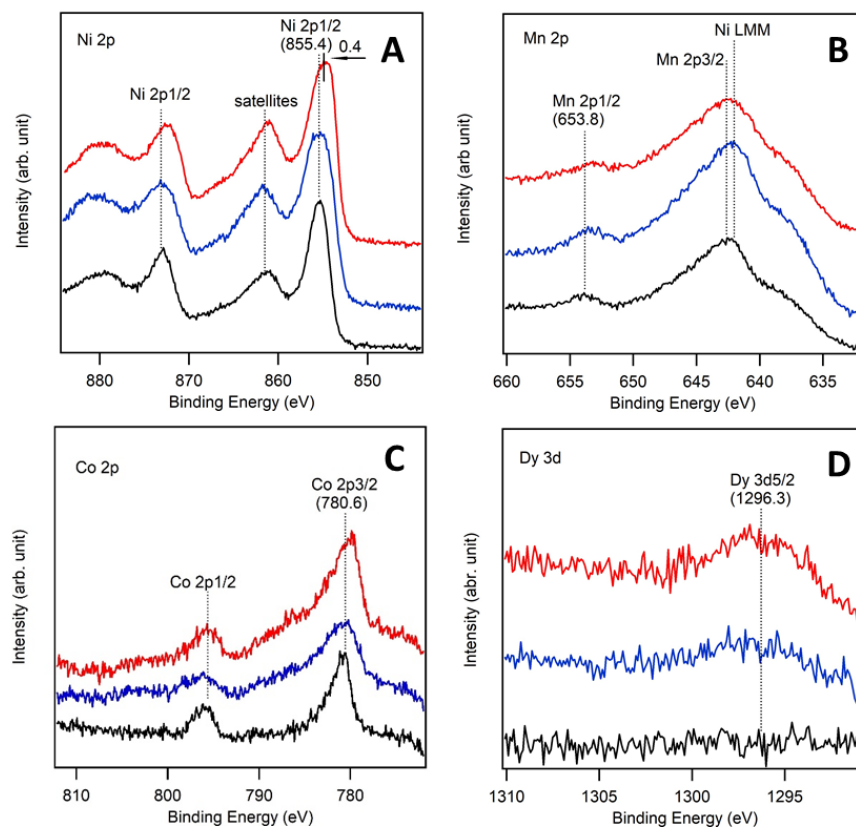


Figure 3. Region scans of XPS spectra for Ni2p, Co2p, Mn2p and Dy 3d for pristine (black), 1.5% Dy-doped (blue), and 3% Dy-doped (red) samples.

The location of the main Ni 2p_{3/2} peak at a binding energy (BE) of 855.4 eV showed the coexistence of Ni²⁺ and Ni³⁺ in all samples, which is consistent with previous research. Although 1.5% Dy doping does not affect the Ni 2p binding energy, increasing Dy doping to 3% slightly shifted the Ni 2p_{3/2} peak to lower binding energy by 0.4 eV. Similar shifting to Co 2p peak was also observed. This result indicates that doped Dy is incorporated into the lattice of the NCM crystal structure and affects the electronic properties.

Table 2. Surface compositions (%) of the samples determined by XPS analysis

	Pristine NCM811	1.5 % Dy	3% Dy
Ni	82.2	69.5	80.9
Co	9.5	10.6	11.4
Mn	8.3	18.1	5.2

3.2. Electrochemical Analysis

Coin cells were fabricated using these synthesized materials as cathodes. The typical initial charge-discharge behaviors and cycle performances were examined at a rate of 0.1C in the potential range from 2.8 to 4.3 V. It can be observed in Figure 4A that all of the curves display stable and smooth charge-discharge behavior without any obvious polarization. NCM811 initially exhibited a discharge capacity of 199.4 mAh g⁻¹, and then with cycling at 1C, its capacity quickly decreased to 137.5 mAh g⁻¹ after 50 cycles as shown in Figure 4B, and only 77 % of the discharge capacity was retained. By comparison, the discharge capacity for Dy-doped electrodes at the first cycle were 197.4 and 193.8 mAh g⁻¹ for Dy-1.5% and Dy-3%, respectively, indicating that an excessive amount of inactive Dy doping is not favorable for the specific capacity of the cell. In the following cycles, however, the discharge capacities were maintained as 167 mAh g⁻¹ (Dy-1.5%), and 165 mAh g⁻¹ (Dy-3%) after 50 cycles, corresponding to reversible capacity retentions of 91.6% and 91.2 %, respectively. The results show that Dy substitution can enhance the cycling property of the NCM811 cathode samples and lower the polarization of the materials.

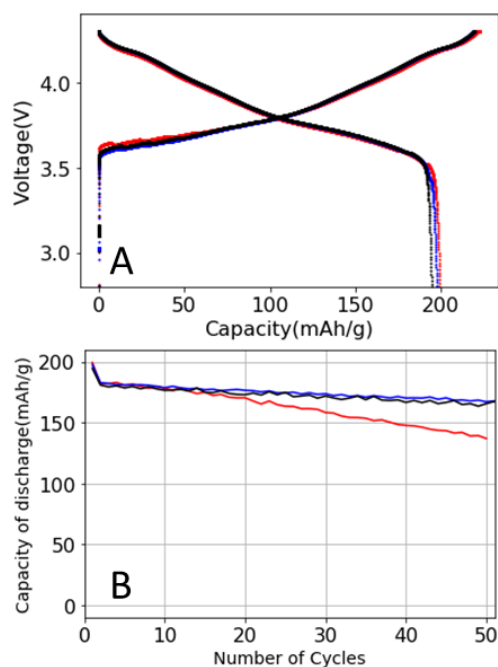


Figure 4. Initial charge/discharge curves (A) and long-term performance (B) of pristine NCM811(red), 1.5%Dy-800°C (blue), and 3%Dy-800°C (black).

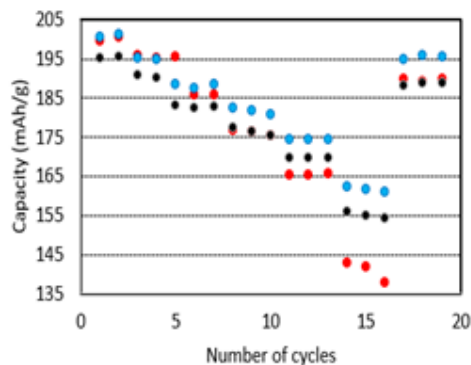


Figure 5. Rate performance of pristine NCM811(Red), 1.5% Dy-800°C (Blue), and 3% Dy-800°C (Black). Rates: 0.1C, 0.2C, 0.5C, 1C, 2C, and 5C. The rate charge-discharge curves are shown in supporting Figure S4.

Figure 5 shows the rate performance of the pristine NCM811 and the Dy doped-NCM811 samples. The charge-discharge measurements were performed using CR2032 coin type cells at current rates of 0.1 C, 0.2C, 0.5C, 1C, 2C, and 5C ($1C = 200 \text{ mA g}^{-1}$) in the voltage range of 2.8-4.3 V for every three cycles, and then the current rate was reduced to 0.1C. The Dy-doped samples exhibited better rate performance than the pristine sample at high rates of current, especially at 5C. The discharge capacity of Dy-1.5 is 165 mAh g^{-1} at 5C, which is about 83% of that at 0.1C, which is a substantial improvement in the rate stability. In comparison, the pristine sample exhibits a capacity 140 g^{-1} at 5C that is about 70% of that at 0.1C. More importantly, when the capacity rate is returned to 0.1C from 5C, the discharge capacity for Dy-doped sample was also greater than that of the pristine sample. The increased capacity of Dy-doped NCM-811 at higher rates could be attributed to the greater $\text{Ni}^{2+}/\text{Ni}^{3+}$ ratio in this material compared to the undoped one. The positive effect of Dy doping is also confirmed by the obvious stabilization of the mean voltage on discharge at high rates.

Cyclic voltammograms (CV) and impedance spectra were obtained on freshly fabricated coin cells to compare the effect of Dy doping on charge transfer of the cathode material. Figure 6A shows the CV curves of pristine NCM811 and 1.5% Dy doped NCM. The battery is scanned at 0.1 mV s^{-1} over the voltage range of 2.8 to 4.3 V. From the CV curves, it can be seen that all of the reduction peaks and oxidation peaks were reversible in the window of 3.6 to 4.0 V for the Dy doped sample. For pristine NCM811, the oxidation peak appears at 3.95 V, and this is related to the Li^+ de-intercalation process and to the oxidation of Ni^{2+} to $\text{Ni}^{3+}/\text{Ni}^{4+}$. The reduction peaks appear at

3.71 and 3.49 V, and this is ascribed to Li^+ intercalation into the cathode materials or the reduction of Ni^{4+} to Ni^{3+} and Ni^{3+} to Ni^{2+} . The appearing of the second reduction peak at 3.49 V may be due to the development of highly resistant SEI layers, causing high overpotentials for the reduction of Ni^{3+} to Ni^{2+} .

The oxidation and reduction peaks of the Dy-doped NCM samples are located at 3.84 and 3.71 V, respectively. As seen in the curves, the oxidation potential decreases by 0.1 V for the Dy-doped sample, suggesting a lower over potential for the reduction reaction. The second redox peaks are located at 4.226/4.15 V or 4.226/4.10 V, corresponding to the phase transformation from H2 (hexagonal phase) to H3 (spinel phase) occurred during Li^+ intercalation/de-intercalation. For the Dy-doped sample, this phase change peak is reduced, indicating that Dy doping can suppress the phase change, although this change cannot be completely eliminated. EIS measurements were carried out for freshly made coin cells to evaluate the resistance and capacitance of charge-transfer. During the measurements, the cells were charged to 4.2 V at 0.1 C and then the voltage was set at 4.2 V in the impedance measurement with 5 mV oscillation. The Nyquist curves plotted in Figure 6 show semicircles and a Warburg diffusion region. The semicircles at high frequency are related to the surface film resistance and its capacitance, and the second semicircle at medium frequency indicates the resistance and capacitance of charge-transfer. For the un-doped NCM811, only one semicircle is present, possibly to due to the large surface film resistance and charge-transfer resistance, that causes these two features to be mixed together. By doping Dy, the resistance for charge-transfer is significantly reduced, which can be deduced from the small semicircles.

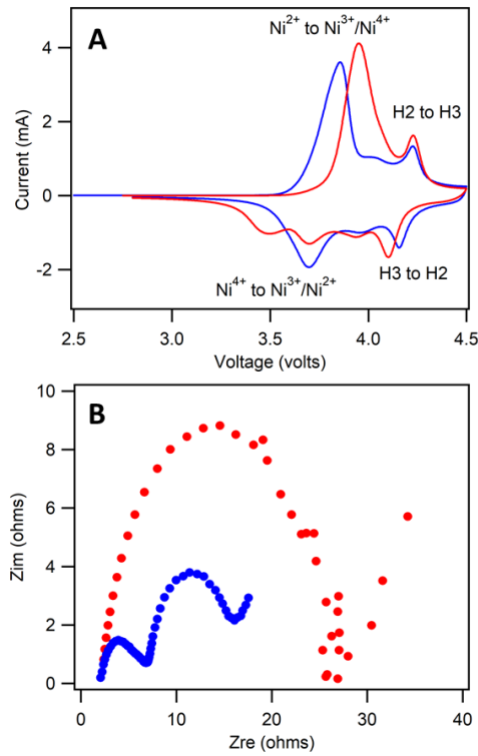


Figure 6. Cyclic voltammetry (A) and impedance spectra (B) of pristine NCM811 (red), 1.5% Dy-800°C (blue). Scan rate: 0.1 V/s, Voltage range: 2.5-4.5 V. Impedance: at 4.2 V with ± 5 mV modulation. Frequency: 0.1-100 kHz.

3.3. Thermal stability

While high-nickel cathode materials typically provide high capacity, [16] the unsatisfactory thermal stability of these materials is a major challenge that needs to be addressed before commercial applications. [17, 18] In this work, the thermal-chemical stability of cathode materials was tested in a micro flow reactor, where charged cathode powders were heated to high temperatures and the gaseous products were detected using a mass spectrometer. As shown in Figure 7, for pristine NCM811, the thermal decomposition product, O₂, was released at 505 K and then developed a broad feature over the temperature range of 505 and 675 K. After Dy-doping, the O₂ onset temperature was shifted to 535 K and total amount of O₂ product decreased by 80%. Therefore, Dy doping strongly stabilizes the crystal structure of NCM811 and suppresses the release of O₂ gas, which is of great significance for improving the thermal stability and creating better fire-resistant lithium ion batteries. [19]

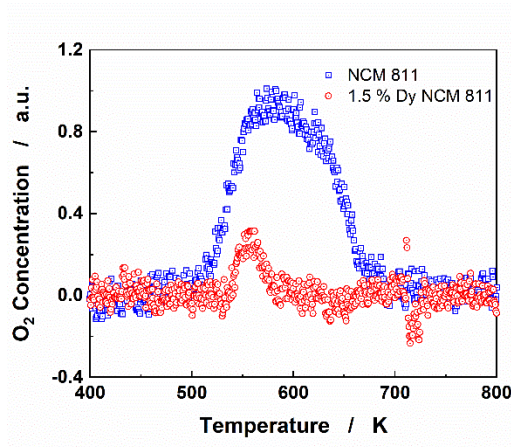


Figure 7. Thermal decomposition profile of charged pristine and 1.5% Dy-doped NCM811.

4. Conclusion

The layered lithium Ni-rich cathode materials, Dy-doped NCM811, were successfully synthesized via an aerosol solid state reaction and subsequent high temperature treatment. XRD results demonstrated that doping NCM811 with a suitable amount of Dy^{3+} reduced the ion mixing, which caused easier Li^+ intercalation/deintercalation in the crystal structure. CV and impedance measurements demonstrated that Dy doped sample had a lower charge-discharge polarization and smaller charge transfer resistance than the pristine sample. Therefore, the long-term cyclability and high-rate performance of the Dy-doped NCM811 electrode was significantly improved. The Dy-doped materials exhibited an excellent rate capability, delivering initial discharge capacities of 199.4 mAh g^{-1} with capacity retentions of 174 mAh \% at 5C, with a cutoff voltage of 4.3 V after 50 cycles. The thermal-chemical stability analysis in a flow reactor showed that Dy doped cathode materials shifted the onset temperature for gas phase O_2 evolution to a higher temperature and reduced O_2 release by 80%, thus showing a dramatically increased thermal-chemical stability and improved fire safety of these cathode materials. However, more experiments are needed to address various unexplained properties of the material, such as the location and role of a LiDyO_2 impurity phase, possible gradient structure, and interaction with the electrolyte. Overall, we have successfully demonstrated the great strength of the high temperature aerosol synthesis approach for controlling ion doping, which enables the improvement of high nickel materials systematically in many different aspects, including long-term cycling, fast discharge, and fire resistance.

Acknowledgments

This work was financially supported by the National Science Foundation under Grant No. 1449314.

BEK acknowledges support of this work by the National Science Foundation under Grant No. CHE-1800376.

Reference

- [1] N. Nitta, F. Wu, J.T. Lee, G. Yushin, Li-ion Battery Materials: Present and Future, *Materials Today*, 18 (2015) 252-264.
- [2] Y. Ding, Z.P. Cano, A. Yu, J. Lu, Z. Chen, Automotive Li-Ion Batteries: Current Status and Future Perspectives, *Electrochemical Energy Reviews*, 2 (2019) 1-28.
- [3] J.B. Goodenough, How We Made the Li-Ion Rechargeable Battery, *Nature Electronics*, 1 (2018) 204.
- [4] C. Zhan, T. Wu, J. Lu, K. Amine, Dissolution, Migration, and Deposition of Transition Metal Ions in Li-Ion Batteries Exemplified by Mn-based Cathodes—A Critical Review, *Energy & Environmental Science*, 11 (2018) 243-257.
- [5] J. Kim, H. Lee, H. Cha, M. Yoon, M. Park, J. Cho, Prospect and Reality of Ni-Rich Cathode for Commercialization, *Advanced Energy Materials*, 8 (2018) 1702028.
- [6] Y. Wu, E. Rahm, R. Holze, Effects of Heteroatoms on Electrochemical Performance of Electrode Materials for Lithium Ion Batteries, *Electrochimica Acta*, 47 (2002) 3491-3507.
- [7] T. Weigel, F. Schipper, E.M. Erickson, F.A. Susai, B. Markovsky, D. Aurbach, Structural and Electrochemical Aspects of $\text{LiNi}_{0.8}\text{Co}_{0.1}\text{Mn}_{0.1}\text{O}_2$ Cathode Materials Doped by Various Cations, *ACS Energy Letters*, 4 (2019) 508-516.
- [8] Z. Chen, D. Chao, J. Lin, Z. Shen, Recent Progress in Surface Coating of Layered $\text{LiNi}_x\text{Co}_y\text{Mn}_z\text{O}_2$ for Lithium-Ion Batteries, *Materials Research Bulletin*, 96 (2017) 491-502.
- [9] M. Shobana, Metal Oxide Coated Cathode Materials for Li-Ion Batteries—A Review, *Journal of Alloys and Compounds*, 802 (2019) 477-487.

- [10] X. Li, K. Zhang, M. Wang, Y. Liu, M. Qu, W. Zhao, J. Zheng, Dual Functions of Zirconium Modification on Improving the Electrochemical Performance of Ni-rich $\text{LiNi}_{0.8}\text{Co}_{0.1}\text{Mn}_{0.1}\text{O}_2$, *Sustainable Energy & Fuels*, 2 (2018) 413-421.
- [11] Y. Ding, P. Zhang, Y. Jiang, D. Gao, Effect of Rare Earth Elements Doping on Structure and Electrochemical Properties of $\text{LiNi}_{1/3}\text{Co}_{1/3}\text{Mn}_{1/3}\text{O}_2$ for Lithium-Ion Battery, *Solid State Ionics*, 178 (2007) 967-971.
- [12] L. Xia, K. Qiu, Y. Gao, X. He, F. Zhou, High Potential Performance of Cerium-Doped $\text{LiNi}_{0.5}\text{Co}_{0.2}\text{Mn}_{0.3}\text{O}_2$ Cathode Material for Li-Ion Battery, *Journal of materials science*, 50 (2015) 2914-2920.
- [13] F. Geoffrey N áCloke, Zero Oxidation State Compounds of Scandium, Yttrium, and the Lanthanides, *Chemical Society Reviews*, 22 (1993) 17-24.
- [14] C. Abram, J. Shan, X. Yang, C. Yan, D. Steingart, Y. Ju, Flame Aerosol Synthesis and Electrochemical Characterization of Ni-Rich Layered Cathode Materials for Li-Ion Batteries, *ACS Applied Energy Materials*, 2 (2019) 1319-1329.
- [15] C. Abram, M. Mezhericher, F. Beyrau, H.A. Stone, Y. Ju, Flame Synthesis of Nanophosphors Using Sub-Micron Aerosols, *Proceedings of the Combustion Institute*, 37 (2019) 1231-1239.
- [16] S. Hwang, S.M. Kim, S.-M. Bak, B.-W. Cho, K.Y. Chung, J.Y. Lee, W. Chang, E.A. Stach, Investigating Local Degradation and Thermal Stability of Charged Nickel-Based Cathode Materials Through Real-Time Electron Microscopy, *ACS applied materials & interfaces*, 6 (2014) 15140-15147.
- [17] S.-M. Bak, E. Hu, Y. Zhou, X. Yu, S.D. Senanayake, S.-J. Cho, K.-B. Kim, K.Y. Chung, X.-Q. Yang, K.-W. Nam, Structural Changes and Thermal Stability of Charged $\text{LiNi}_x\text{Mn}_y\text{Co}_z\text{O}_2$ Cathode Materials Studied by Combined *in situ* Time-Resolved XRD and Mass Spectroscopy, *ACS Applied Materials & Interfaces*, 6 (2014) 22594-22601.
- [18] F. Schipper, E.M. Erickson, C. Erk, J.-Y. Shin, F.F. Chesneau, D. Aurbach, Recent Advances and Remaining Challenges for Lithium Ion Battery Cathodes I. Nickel-Rich, $\text{LiNi}_x\text{Co}_y\text{Mn}_z\text{O}_2$, *Journal of The Electrochemical Society*, 164 (2017) A6220-A6228.
- [19] Q. Wang, P. Ping, X. Zhao, G. Chu, J. Sun, C. Chen, Thermal Runaway Caused Fire and Explosion of Lithium Ion Battery, *Journal of Power Sources*, 208 (2012) 210-224.

List of Supplemental Materials

1. Supporting Experimental Details
2. Supporting Results